

Constraining the Secluded and Catalyzed Annihilation Dark Matter with Fermi-LAT and Planck Data

Yu-Hang Su^a, Chengfeng Cai^{b,*} and Hong-Hao Zhang^{a†}

^a*School of Physics, Sun Yat-sen University, Guangzhou 510275, China and*

^b*School of Science, Sun Yat-Sen University, Shenzhen 518107, China*

We propose a dark matter (DM) model with a complex scalar charged under a hidden gauge symmetry, denoted as $U(1)_D$. The scalar field is the DM candidate while the $U(1)_D$ gauge field A' plays the role of a mediator, which connects the dark sector to the standard model (SM) sector via a tiny kinetic mixing. We find that both the secluded and catalyzed annihilation scenarios can be realized in this model. The phenomenology of DM, including relic density, indirect detection (Fermi-LAT), and CMB (Planck) constraints, is discussed. We also extend our discussion to DM with other spins, including Dirac fermion and vector boson. Our analysis is carried out in two models, denoted as $U(1)_D \times U(1)_Y$ and $U(1)_D \times U(1)_{L_\mu-L_\tau}$, with the former corresponding to A' kinetically mixing with the $U(1)_Y$ gauge field B and the latter corresponding to A' mixing with the $U(1)_{L_\mu-L_\tau}$ gauge field Z' . In previous studies of catalyzed annihilation scenarios, we find that the indirect detection limits were overly restrictive because they only considered the simplified $2DM \rightarrow 2SM$ annihilation channel. In contrast, by performing a complete calculation of the gamma-ray and CMB constraints from the process $2DM \rightarrow 2A' \rightarrow 4SM$ in the models we consider, we observe weaker constraints in both the $U(1)_D \times U(1)_Y$ and $U(1)_D \times U(1)_{L_\mu-L_\tau}$ models, with the $U(1)_D \times U(1)_{L_\mu-L_\tau}$ model being subject to the weakest constraints overall since it involves fewer hadronic decay processes.

CONTENTS

I. Introduction	2
II. Dark Matter Models	3
A. Complex Scalar DM	4
B. Dirac fermionic DM	8
C. Vector Boson DM	8
III. Dark Matter Phenomenology	9
A. Gamma rays	10
B. Cosmic Microwave Background	14
IV. Results	15
V. Conclusions	18

* Corresponding author. caichf3@mail.sysu.edu.cn

† Corresponding author. zhh98@mail.sysu.edu.cn

Acknowledgments	20
A. J-factors for the Benchmark Sample	20
B. Kinetic Equilibrium Before DM Freeze-out	21
References	22

I. INTRODUCTION

Dark matter (DM) is believed to constitute about 27% of total energy density of our universe, supported by numerous astrophysical and cosmological evidence despite its unknown nature [1–4]. It is well known that Weakly Interacting Massive Particles (WIMPs), with masses from GeV to TeV scale and couplings similar to the weak interaction, are promising candidates for DM, since they can naturally reproduce the correct relic abundance via thermal freeze-out in the early universe [5]. Various direct detection experiments have been developed to search for WIMPs, such as XENONnT [6], PandaX-4T [7] and LUX-ZEPLIN (LZ) [8]. Since no conclusive signals have been confirmed so far, direct searches place increasingly stringent constraints on WIMPs [9, 10]. Therefore, many models beyond typical WIMPs have been proposed, such as Strongly Interaction Massive Particles (SIMPs) [11–13], Forbidden and Not-Forbidden DM [14–16], Secluded and Catalyzed DM [17–21], and so on.

For the secluded DM model, the DM particles mainly annihilate into some lighter non-SM mediators, denoted as A' , which then decay into SM particles after DM freeze-out. In this case, the $2 \rightarrow 2$ DM annihilation processes are accomplished within the dark sector, so the annihilation strength is no longer correlated with the scattering strength between DM and nucleons. In particular, if the mediator is long-lived and its coupling to DM is sufficiently strong, the $3A' \rightarrow 2\text{DM}$ process would play an important role when it is allowed kinematically. In this case, a new process, called catalyzed annihilation [20, 21], occurs: three $2\text{DM} \rightarrow 2A'$ processes accompanied with two $3A' \rightarrow 2\text{DM}$ processes, effectively leading to a $6\text{DM} \rightarrow 4\text{DM}$ process. In this scenario, the yield of DM decreases in a manner of $x^{-3/2}$ rather than e^{-x} . This leads to a much lower freeze-out temperature of DM comparing to the usual WIMP scenario. On the other hand, if the mass relation is inverse, $m_{A'} > m_\chi$, it becomes the Forbidden or Not-Forbidden DM scenario. Particularly, Refs. [15, 16] also discuss different freeze-out pictures when $\Gamma_{A'}$ ranges large to small. Note that the (Not-)Forbidden DM models mainly focus on sub-GeV DM, while the secluded and catalyzed DM models study the scale from GeV to TeV, which is also the mass range for the typical WIMPs DM models.

In this work, we propose a complex scalar DM model involving a hidden gauge symmetry, $U(1)_D$. Complex scalar DM models have been discussed in many previous studies [22–26]. We consider a complex scalar Φ charged under $U(1)_D$ as the DM candidate while the gauge boson A' of $U(1)_D$ mediates interactions between the dark and SM sectors via the kinetic mixing. Both secluded and catalyzed scenarios can be realized in this model. We consider the DM

phenomenology including relic density, gamma-ray bounds from Fermi-LAT, and CMB bounds from Planck experiment. The Fermi-LAT constraints are derived from a combined analysis of 14.3 years of observations on 42 dwarf galaxies, while the CMB constraints are based on the Planck 2018 results. For comprehensiveness, we also extend our discussion of DM phenomenology to the fermionic and vector DM models. In most of the previous studies, indirect detection constraints were usually obtained by considering a single $2\text{DM} \rightarrow 2\text{SM}$ annihilation channel (e.g., W^+W^- or $b\bar{b}$). However, this treatment is oversimplified in the secluded or catalyzed annihilation scenarios, leading to an overly stringent limit on the parameter space. Therefore, a goal of this work is to perform a more careful determination of the latest Fermi-LAT and CMB constraints, based on a full analysis of $2\text{DM} \rightarrow 2A' \rightarrow 4\text{SM}$ channels. These calculations are carried out under two different models, denoted as $U(1)_D \times U(1)_Y$ and $U(1)_D \times U(1)_{L_\mu-L_\tau}$. The main difference between these models is the portal connecting the dark sector to the SM sector. We present the phenomenological constraints on these two models and apply them to the secluded and catalyzed annihilation scenarios for DM with different spins.

It is worth noting that some previous studies have also discussed the indirect detection constraints for the secluded DM based on the $2\text{DM} \rightarrow 2A' \rightarrow 4\text{SM}$ channels [27–30]. However, they mainly focus on single annihilation channels such as $4e$, 4μ , 4τ , or others. In contrast, the two models we consider, involve multiple decay channels of the mediator A' , resulting in different gamma-ray spectra of final state particles.

This paper is organized as follows. In Sect. II, we introduce the secluded and catalyzed DM with different spins, including complex scalar, Dirac fermion and vector boson. In Sect. III, we introduce the $U(1)_D \times U(1)_Y$ and $U(1)_D \times U(1)_{L_\mu-L_\tau}$ models and how we derive the constraints from Fermi-LAT and Planck. In Sect. IV, we present the limits and allowed parameter space for each DM spin. In the end, we draw our conclusions in Sect. V.

II. DARK MATTER MODELS

In this section, we investigate the secluded and catalyzed models for DM with different spins: 0 (complex scalar), 1/2 (Dirac fermion), and 1 (vector boson). We focus on the cases that DM interacts with SM particles via vector portal. The mediator is a gauge boson denoted by A' , and dark matters deplete through the process $2\text{DM} \rightarrow 2A' \rightarrow 4\text{SM}$ (see Fig. 1), and thus the mass of A' should be smaller than the DM mass, i.e., $m_{A'} \lesssim m_\chi$. If A' decays promptly when they are created, the situation would be very similar to the traditional WIMPs paradigm, except that the relic density of DM is determined by the DM- A' coupling which is free from the constraint of direct detection. This scenario will be called secluded DM model in this work. On the other hand, if the decay width of A' , denoted as $\Gamma_{A'}$, is extremely small, it will lead to the catalyzed annihilation DM scenario, which will be called catalyzed model for short.¹ Fig. 2 illustrates how the catalyzed annihilation mechanism works to achieve the depletion of DM.

¹ Strictly speaking, the catalyzed model can be considered a type of secluded model since its DM particle is also hidden in the dark sector. However, to make a distinction in this paper, we refer to the case that only considers the $2 \rightarrow 2$ process as secluded, while the case that simultaneously considers the $3 \rightarrow 2$ process is referred to as catalyzed model.

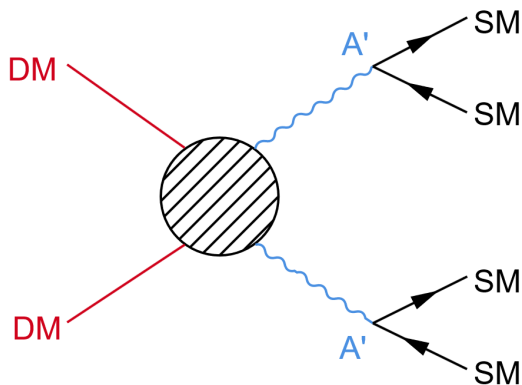


FIG. 1. Feynman diagram for DM annihilating into mediator A' , which then decays into SM particles.

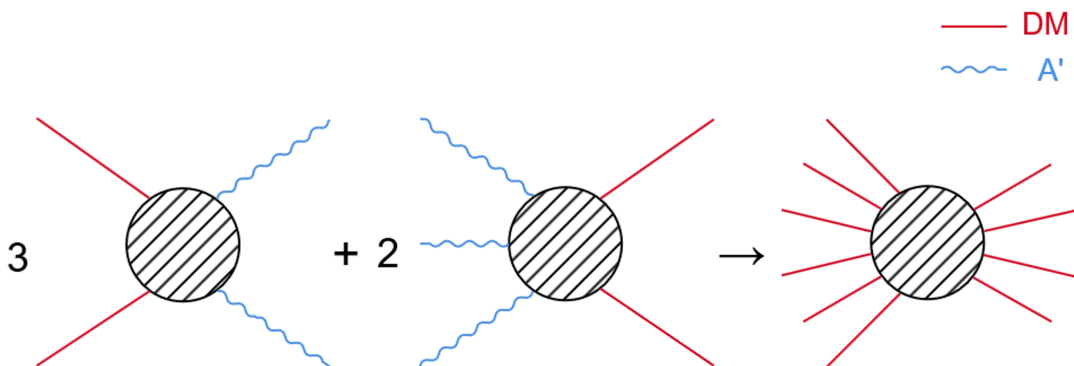


FIG. 2. Feynman diagrams for catalyzed annihilation of DM with catalyst A' . The reduction of DM is realized through three $2DM \rightarrow 2A'$ plus two $3A' \rightarrow 2DM$, eventually resulting in a $6DM \rightarrow 4DM$ process.

Studies of model building and DM relic density for the fermionic and vector DM have been provided in [20] and [21], respectively. The constraints from indirect detection are also discussed in these papers, however, their analysis is overly simplified. Therefore, in this work, we will offer a detailed discussion on the setup of complex scalar DM model, and provide a more accurate and comprehensive treatment of indirect detection constraints.

A. Complex Scalar DM

The simplest model for complex scalar DM is the $U(1)_D$ dark photon model, where DM Φ is charged under $U(1)_D$ and A' is the $U(1)_D$ gauge boson. The Lagrangian for the dark sector is given by,

$$\mathcal{L}_D^{(0)} = -\frac{1}{4}F'^{\mu\nu}F'_{\mu\nu} + \frac{1}{2}m_{A'}^2 A'^\mu A'_\mu + (D^\mu \Phi)^\dagger D_\mu \Phi - m_\Phi^2 |\Phi|^2 - \lambda_\Phi |\Phi|^4 - \lambda_{\Phi H} |\Phi|^2 |H|^2, \quad (1)$$

where the covariant derivative is defined as $D_\mu = \partial_\mu - ig_D A'_\mu$. The superscript (0) in $\mathcal{L}_D^{(0)}$ denotes the spin of DM. The mass of A' can be generated through the Brout-Englert-Higgs mechanism or the Stueckelberg mechanism. Since we only focus on the vector-portal process,

we assume $\lambda_{H\Phi}$ to be negligible, and thus the Higgs-portal annihilation or scattering processes are suppressed. Otherwise, the model would no longer be secluded but instead become the normal WIMP paradigm.

When $m_{A'} \lesssim m_\chi$, the dominant annihilation channels are: $2\Phi \rightarrow 2A'$ and $3A' \rightarrow 2\Phi$. The Boltzmann equations of Φ and A' are given by, ²

$$\frac{dn_\Phi}{dt} + 3Hn_\Phi = -\frac{1}{2}\langle\sigma_2v\rangle\left(n_\Phi^2 - \bar{n}_\Phi^2\frac{n_{A'}^2}{\bar{n}_{A'}^2}\right) + 2\langle\sigma_3v^2\rangle\left(n_{A'}^3 - \bar{n}_{A'}^3\frac{n_\Phi^2}{\bar{n}_\Phi^2}\right), \quad (2)$$

$$\frac{dn_{A'}}{dt} + 3Hn_{A'} = \frac{1}{2}\langle\sigma_2v\rangle\left(n_\Phi^2 - \bar{n}_\Phi^2\frac{n_{A'}^2}{\bar{n}_{A'}^2}\right) - 3\langle\sigma_3v^2\rangle\left(n_{A'}^3 - \bar{n}_{A'}^3\frac{n_\Phi^2}{\bar{n}_\Phi^2}\right) - \Gamma_{A'}(n_{A'} - \bar{n}_{A'}), \quad (3)$$

where $\langle\sigma_2v\rangle$ and $\langle\sigma_3v^2\rangle$ are the thermally averaged cross sections of $2\Phi \rightarrow 2A'$ and $3A' \rightarrow 2\Phi$, respectively. n_Φ represents the total number density of DM Φ and anti-DM Φ^\dagger , while $\bar{n}_{\Phi, A'}$ denote the equilibrium densities.

The Feynman diagrams of $2\Phi \rightarrow 2A'$ and $3A' \rightarrow 2\Phi$ are shown in Fig. 3 and Fig. 4, respectively. In the kinematic threshold limit, which is equivalent to adopting a non-relativistic approximation keeping only the leading-order terms, their thermally averaged cross sections can be obtained using the formulas (E4) and (E5) in [15], which yield the following results:

$$\langle\sigma_2v\rangle = \frac{g_D^4(8r^4 - 8r^2 + 3)}{16\pi m_\Phi^2(1 - 2r^2)^2}\sqrt{1 - \frac{1}{r^2}}, \quad (4)$$

$$\langle\sigma_3v^2\rangle = \frac{g_D^6 r^5(-64r^6 + 368r^4 - 716r^2 + 477)}{1536\pi m_\Phi^5}\sqrt{9 - 4r^2}, \quad (5)$$

where $r \equiv m_\Phi/m_{A'}$.

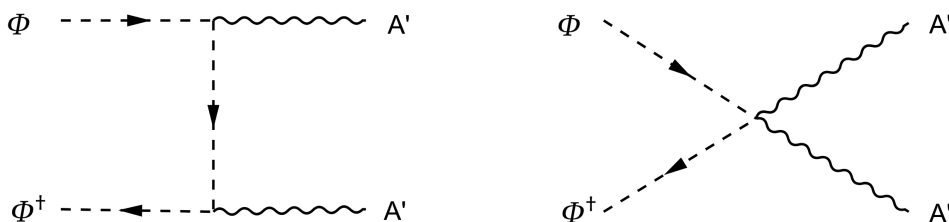


FIG. 3. Feynman diagrams of $2\Phi \rightarrow 2A'$ process. Note that the first plot includes t- and u-channels, which can be obtained by exchanging the external lines of A' .

A' can mix with other gauge bosons via kinetic term, making it unstable and causing it to eventually decay into SM particles. The simplest realization is to let A' mix with the $U(1)_Y$ gauge field B :

$$\mathcal{L}_{\text{kin}} \supset -\frac{s_\epsilon}{2}F'_{\mu\nu}B^{\mu\nu}, \quad (6)$$

² Pay attention to the different conventions for $\langle\sigma_2v\rangle$ and $\langle\sigma_3v^2\rangle$ used in [15, 20, 21]. For example, Ref. [15] includes the symmetry factor for initial identical particles in the Boltzmann equation, while Ref. [21] absorbs it into the cross sections. In this work, we adopt the convention used in [21].

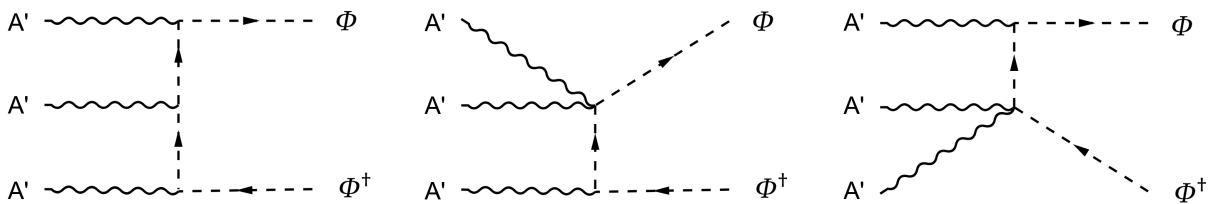


FIG. 4. Feynman diagrams of $3A' \rightarrow 2\Phi$ process. Similarly, by exchanging the external lines of A' , the first plot has 6 independent diagrams, while the latter two each have 3 independent diagrams.

where $F'^{\mu\nu}$ is the field strength tensor of A' . This realization, which we denote as the $U(1)_D \times U(1)_Y$ model, can also induce scattering between DM and nuclei. The Φ -proton cross section can be estimated using effective field theory [31, 32]:

$$\sigma_{V,\Phi p} \simeq \frac{m_p^2}{\pi} \left(\frac{ec_W g_D s_\epsilon}{m_{A'}^2} \right)^2. \quad (7)$$

Comparing it to the latest direct detection bound from the LZ experiment [8], $\sigma_{\text{SI}} \sim 3 \times 10^{-47} \text{ cm}^2$ for 1 TeV DM, we find that the kinetic mixing angle is constrained to be:

$$s_\epsilon \lesssim 2 \times 10^{-3} \left(\frac{1}{g_D} \right) \left(\frac{m_\Phi}{1 \text{ TeV}} \right)^2, \quad (8)$$

assuming $m_{A'} \approx m_\Phi$. In the following discussion of several benchmarks, the parameters are chosen to satisfy this bound. In addition, since $s_\epsilon \ll 1$, we can safely treat A' as its mass eigenstate. The decay width of A' induced by the kinetic mixing can be simply estimated as [33]:

$$\Gamma_{A'} \simeq \frac{27\alpha s_\epsilon^2 m_{A'}}{16c_W^2} \simeq 2 \times 10^{-2} s_\epsilon^2 m_{A'}. \quad (9)$$

Fig. 5 illustrates the thermal evolution of DM Φ (solid red) and mediator A' (solid blue) as the temperature decreases for benchmark models with $s_\epsilon = 10^{-10}$ (5(a)), 2×10^{-9} (5(b)), and 10^{-6} (5(c)). The gauge coupling g_D is adjusted to 1.3, 1.03, and 0.62 respectively, in order to reproduce the observed DM relic abundance, $\Omega_{\text{DM}} h^2 = 0.12$ [34]. Other parameters are fixed as follows: $m_\Phi = 10^3 \text{ GeV}$ and $r = 1.2$. Fig. 5(a) depicts a complete catalyzed annihilation process until DM freeze-out, without termination from A' decay. Fig. 5(b) illustrates the scenario where an increased s_ϵ ($\Gamma_{A'}$) leads to the sudden termination of the catalyzed annihilation processes via the decay of A' . This forces the DM to freeze out earlier. We refer to this as a semi-catalyzed annihilation compared to the former case. Fig. 5(c) corresponds to a standard $2 \rightarrow 2$ freeze-out process without catalyzed annihilation. In this case, A' remains in thermal equilibrium and never freezes out, making the model reduce to a secluded one. Comparing the plots in Fig. 5, we can see that g_D decreases with increasing s_ϵ for maintaining the correct relic abundance. This can be expected since the depletion of DM in the catalyzed annihilation scenario is less efficient than the usual secluded scenario, thus a larger g_D is required to enhance the annihilation rate

of DM.

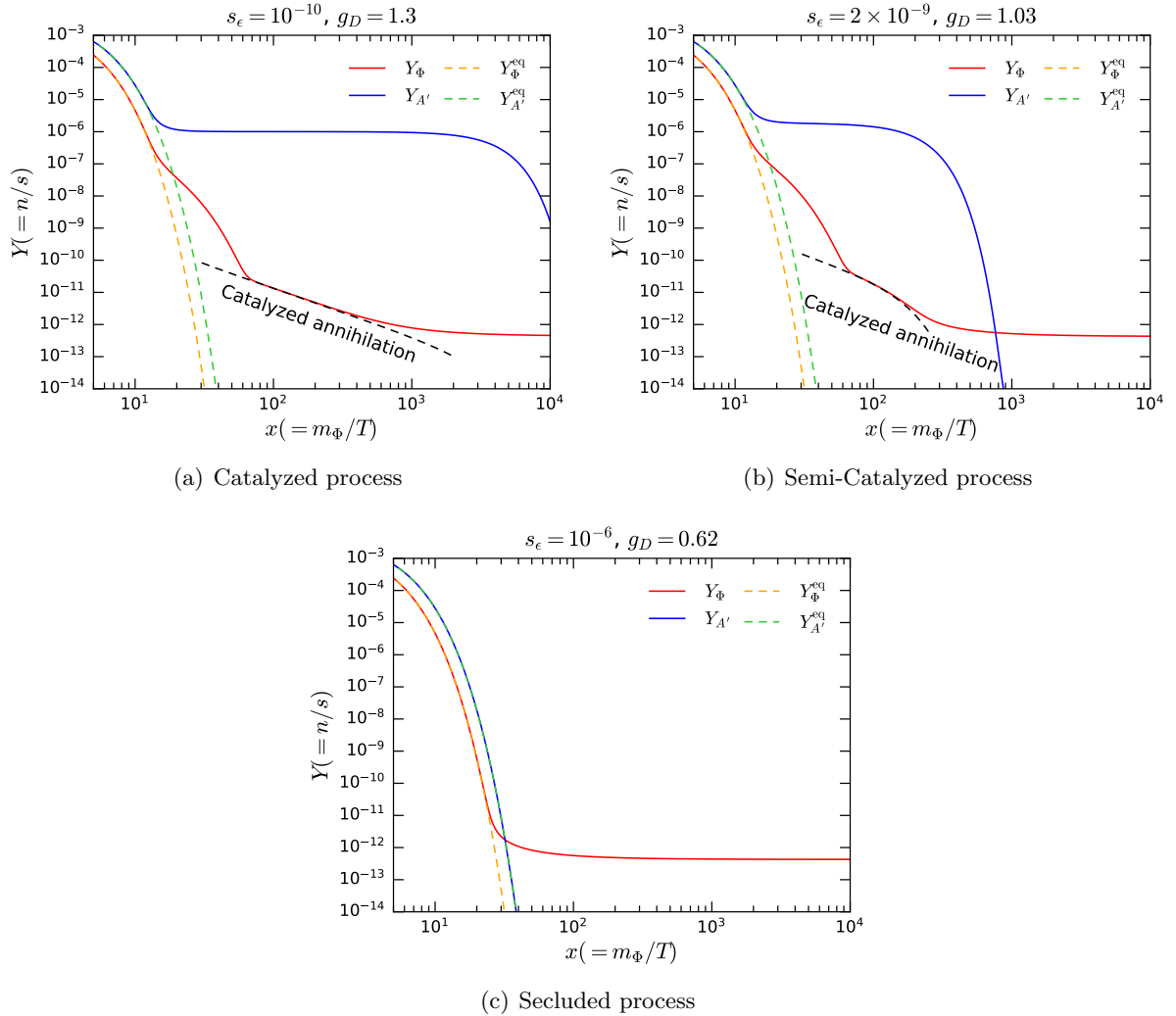


FIG. 5. The evolution of the yields of DM Φ (solid red) and mediator A' (solid blue) for $s_\epsilon = 10^{-10}$ (top left panel), 2×10^{-9} (top right panel), and 10^{-6} (bottom panel). The gauge coupling g_D is chosen to be 1.3, 1.03, and 0.62 respectively, to obtain the correct DM relic abundance, $\Omega_\Phi h^2 = 0.12$. As s_ϵ increases, the catalyzed annihilation is terminated earlier by A' decay, thus the model reduces to a secluded one eventually.

We note that with such a small mixing angle s_ϵ , maintaining kinetic equilibrium (KE) between the dark sector and the SM sector becomes difficult. To address this issue, we present a method in Appendix B to keep DM in KE until freeze-out, ensuring temperature equality between the dark and SM sectors.

B. Dirac fermionic DM

We can also consider the DM to be a Dirac fermion, which is charged under the $U(1)_D$ gauge symmetry. In this case, the Lagrangian for the dark sector becomes:

$$\mathcal{L}_D^{(1/2)} = -\frac{1}{4}F'^{\mu\nu}F'_{\mu\nu} + \frac{1}{2}m_{A'}^2 A'^{\mu}A'_{\mu} + \bar{\chi}(i\not{D} - m_{\chi})\chi. \quad (10)$$

The annihilation cross sections of $2\chi \rightarrow 2A'$ and $3A' \rightarrow 2\chi$ processes are given by [15],

$$\langle\sigma_2 v\rangle = \frac{g_D^4(r^4 - r^2)}{4\pi m_{\chi}^2(1 - 2r^2)^2} \sqrt{1 - \frac{1}{r^2}}, \quad (11)$$

$$\langle\sigma_3 v^2\rangle = \frac{g_D^6 r^5(24r^6 - 60r^4 - 47r^2 + 153)}{2592\pi m_{\chi}^5} \sqrt{9 - 4r^2}. \quad (12)$$

The Boltzmann equations have the same form as Eqs. (2), except that Φ is replaced by χ .

C. Vector Boson DM

We can also consider the DM to be a complex vector field X_{μ} . In this case, both the DM and mediator are vector fields, and thus an elegant realization is to unify the DM and the mediator by an $SU(2)_D$ gauge symmetry [21]. The DM X and the mediator A' stem from the components of the $SU(2)_D$ gauge fields, V_{μ}^a ($a = 1, 2, 3$). To be precise, the DM field is defined as $X_{\mu} = (V_{\mu}^1 - iV_{\mu}^2)/\sqrt{2}$, while the mediator is $A'_{\mu} = V_{\mu}^3$. Their masses can be generated by the Brout-Englert-Higgs mechanism via non-zero vacuum expectation values (VEVs) of a doublet Φ_D and a real triplet Δ_D scalar fields. In this scenario, the Lagrangian for the dark sector is given by,

$$\mathcal{L}_D^{(1)} = -\frac{1}{4}V_{\mu\nu}^a V^{a,\mu\nu} + (D^{\mu}\Phi_D)^{\dagger}D^{\mu}\Phi_D + \text{Tr}[(D^{\mu}\Delta_D)^{\dagger}D^{\mu}\Delta_D] - V(\Phi_D, \Delta_D), \quad (13)$$

where $V(\Phi_D, \Delta_D)$ is the potential terms of the new scalar fields. The potential is assumed to have a form such that both Φ_D and Δ_D acquire non-zero VEVs. In this situation, the DM is heavier than the mediator automatically. The cross sections of $2X \rightarrow 2A'$ and $3A' \rightarrow 2X$ processes are given by [21],

$$\langle\sigma_2 v\rangle = \frac{g_D^4(152r^4 - 136r^2 + 128 - 18r^{-2} + 3r^{-4})}{144\pi m_X^2(1 - 2r^2)^2} \sqrt{1 - r^{-2}}, \quad (14)$$

$$\langle\sigma_3 v^2\rangle = \frac{g_D^6 r^5 f(r)}{3456\pi m_X^5} \sqrt{9 - 4r^2}, \quad (15)$$

$$f(r) = -48r^6 - 12r^4 + 415r^2 - \frac{2317}{4} + \frac{2585}{4}r^{-2} - \frac{1007}{4}r^{-4} + \frac{1285}{8}r^{-6} + \frac{675}{16}r^{-8} - \frac{243}{16}r^{-10} + \frac{729}{256}r^{-12}. \quad (16)$$

In the $SU(2)_D$ model, the kinetic mixing between A' and the $U(1)_Y$ gauge field B_{μ} can be

realized through a dimension-5 effective operator:

$$\mathcal{L}_5 = -\frac{c}{\Lambda} B^{\mu\nu} \Delta_D^a V_{\mu\nu}^a \supset -\frac{s_\epsilon}{2} F'_{\mu\nu} B^{\mu\nu}, \quad (17)$$

where c is a Wilson coefficient, and Λ represents a UV complete scale. This term can generate the same kinetic mixing term as in the $U(1)_D$ model. Consequently, the decay width and decay channels of A' are identical to those in the $U(1)_D$ model.

The Boltzmann equations for DM and mediator particles have the same form as Eqs. (2), except that Φ is replaced by X .

III. DARK MATTER PHENOMENOLOGY

In this section, we investigate the astrophysical signatures arising from the annihilation of secluded or catalyzed DM. Searching for these DM directly would be difficult if the kinetic mixing parameter is extremely small, since the cross section of DM-nucleon scattering depends on the mixing directly. On the other hand, the annihilation cross section of DM is dominated by $\bar{\chi} - \chi - A'$ coupling, which can be significant. Therefore, indirect detections of DM might play a crucial role in DM searches. For instance, gamma-ray flux can be generated by the charged products originating from A' decay. In this case, the production rate of A' , which is determined by the annihilation cross section of the $2\text{DM} \rightarrow 2A'$ process, is the most relevant quantity.

In the $U(1)_D \times U(1)_Y$ model³ A' can decay into various final states, including quark-antiquark pairs $q\bar{q}$ ($q = u, d, s, c, b, t$), charged leptons $l\bar{l}$ ($l = e, \mu, \tau$), neutrinos $\nu\bar{\nu}$ ($\nu = \nu_e, \nu_\mu, \nu_\tau$), W^+W^- , and Z or h bosons. When we consider the annihilation chain processes $2\chi \rightarrow 2A' \rightarrow 4\text{SM}$, the situation becomes more complicated. Although the `PPPC4DM` code provides gamma-ray spectra for pure channels like $2\chi \rightarrow 2V \rightarrow 4e, 4\mu, 4\tau$ [35], it cannot be directly applied to our model, since in addition to pure channels like $2\chi \rightarrow 4q, 4l, 4\nu$, there are also mixed channels such as $2\chi \rightarrow 2q2l, 2q2\nu, 2l2\nu, 2qW^+W^-, 2qZh$, etc.. After determining the hadronization, these processes may lead to intricate distributions of the kinetic energies of final-state particles. Moreover, `PPPC4DM` assumes that the mediator is only slightly heavier than its decay products (usually much lighter than the DM), whereas in our model, A' is just slightly lighter than DM. Given these considerations, we utilize the `Pythia8` [36] event generator to obtain the gamma-ray spectra in our work. Moreover, since `Pythia8` now directly supports electroweak (EW) showers to simulate the soft radiation of EW gauge bosons, it allows us to incorporate EW corrections into the calculations of gamma-ray spectra and indirect detection constraints.

Since A' in the $U(1)_D \times U(1)_Y$ model can decay into hadronic final states, it produces more gamma rays comparing to pure leptonic decays. On the other hand, if we consider a model where A' dominantly decays into leptons, then the constraints from indirect detections will be released. In this work, we will consider an extension of SM with $U(1)_D \times U(1)_{L_\mu - L_\tau}$ gauge symmetries, and the mediator field A' kinetically mixes with the gauge boson, Z' , corresponding

³ For the vector DM introduced in Sect. II C, it should be the $SU(2)_D \times U(1)_Y$ model. For convenience, we use $U(1)_D$ to represent the three types of DM introduced in Sect. II throughout this work. In Sect. IV, we use current indirect detection bounds to constrain all these three types of DM.

to the $U(1)_{L_\mu-L_\tau}$ gauge symmetry. The $U(1)_{L_\mu-L_\tau}$ model has various potential implications. For instance, it may provide an explanation for the electron and muon ($g-2$) anomalies [37–39]. Additionally, it could lead to the production of dark photons at the MUonE experiment [40]. Moreover, it may help to interpret the excess of electrons and positrons observed in cosmic-ray measurements [41, 42].

The kinetic mixing term in this extended model changes from Eq. (6) to:

$$\mathcal{L}'_{\text{kin}} \supset -\frac{s'_\epsilon}{2} F'_{\mu\nu} Z'^{\mu\nu}, \quad (18)$$

where $Z'^{\mu\nu}$ is the field strength tensor of Z' . The Lagrangian for the Beyond the Standard Model (BSM) sector becomes:

$$\mathcal{L}'_{BSM} = \mathcal{L}'_D^{(S)} - \frac{1}{4} Z'^{\mu\nu} Z'_{\mu\nu} + \frac{1}{2} m_{Z'}^2 Z'^\mu Z'_\mu + g_x J_\nu^x Z'^\nu, \quad (19)$$

where the superscript (S) denotes the spin of DM and g_x denotes the $U(1)_{L_\mu-L_\tau}$ gauge coupling. The current J_ν^x is given by,

$$J_\nu^x = \bar{L}_\mu \gamma_\nu L_\mu + \bar{\mu}_R \gamma_\nu \mu_R - \bar{L}_\tau \gamma_\nu L_\tau - \bar{\tau}_R \gamma_\nu \tau_R. \quad (20)$$

In this model, A' dominantly decays into leptonic final states, including μ pairs, τ pairs, and corresponding neutrino partners via the current J_ν^x . As a result, A' has only four decay channels in this model, making it much simpler than the $U(1)_D \times U(1)_Y$ model. We also use `Pythia8` to obtain its gamma-ray spectra.

It is worth noting that the model-building approach for the $U(1)_D \times U(1)_{L_\mu-L_\tau}$ model can be extended to other $U(1)'$ models, such as $U(1)_{L_\mu-L_e}$, $U(1)_{L_e-L_\tau}$, and $U(1)_{B-L}$. The decay channels of A' vary across these models, leading to different gamma-ray spectra. Consequently, the constraints from indirect searches are model-dependent. In some previous studies, constraints of gamma rays are often derived from $2\text{DM} \rightarrow 2\text{SM}$ processes in a single annihilation channel (e.g., W^+W^- or $b\bar{b}$). However, this treatment is oversimplified for secluded or catalyzed annihilation DM models, since the actual processes are $2\text{DM} \rightarrow 4\text{SM}$ processes. The approach employed in this work, which considers the full decay spectra of A' via numerical simulation, can derive much more accurate results.

A. Gamma rays

DM particles can continuously self-annihilate to produce SM particles, especially in regions with high DM density. Stable products like positrons, electrons, and gamma rays can be observed by telescopes like the Fermi Large Area Telescope (Fermi-LAT), which detects gamma-ray data from the Milky Way's dwarf spheroidal galaxies (dSphs). dSphs are regarded as perfect sources for DM searches due to their proximity, DM dominance, and low astrophysical background, which minimize contamination from non-DM sources. Since no significant DM annihilation

signal from dSphs has been observed so far, these observations have placed tight constraints on the annihilation cross sections for various DM annihilation channels [43–46].

We utilize the Fermi-LAT 2023 data from the P8R3SOURCEV3 event class, based on 14.3 years of observations of 42 dSphs [44]⁴. The data covers an energy range from 500 MeV to 1 TeV, with likelihoods extracted for each energy bin. The collaboration has made these likelihood functions publicly available⁵, enabling researchers to perform joint likelihood analyses across multiple dSphs for any given gamma-ray spectrum.

The expected differential gamma-ray flux from DM annihilation in a given angular direction ($\Delta\Omega$) is given by [35],

$$\frac{d\Phi}{dE}(\Delta\Omega) = \frac{1}{4\pi\eta} \frac{\langle\sigma v\rangle}{m_{\text{DM}}^2} \left(\frac{dN}{dE}\right)_\gamma \cdot J, \quad (21)$$

where $\langle\sigma v\rangle$ is the thermal annihilation cross section of DM, and $\left(\frac{dN}{dE}\right)_\gamma$ is the average gamma-ray energy spectrum per annihilation. The factor $\eta = 2$ (4) corresponds to self-conjugate (non-self-conjugate) DM, and in this work, we consider non-self-conjugate DM models. The astrophysical J-factor J is given by,

$$J = \int_{\Delta\Omega} d\Omega \int_{\text{l.o.s.}} ds \rho_{\text{DM}}^2(s), \quad (22)$$

where the integrals run over $\Delta\Omega$ and the line-of-sight (l.o.s.) through the DM distribution. We employ the DM density Navarro-Frenk-White (NFW) profile here [48], which aligns with the choice of Fermi-LAT collaboration. The profile reads,

$$\rho_{\text{DM}} = \frac{\rho_0 r_s^3}{r(r_s + r)^2}, \quad (23)$$

where ρ_0 is the characteristic density and r_s is the scale radius. It should be noted that adopting other profiles, such as a steeper profile [49] or a more core-like profile [50, 51], would result in a shift of our limits by a constant factor.

In the secluded and catalyzed annihilation scenarios, the model-dependent part in Eq. (21) is the energy spectrum $(dN/dE)_\gamma$, which can be computed by `Pythia8`. In Fig. 6, we present gamma-ray spectra for the $U(1)_{\text{D}} \times U(1)_{\text{Y}}$ and $U(1)_{\text{D}} \times U(1)_{L_\mu-L_\tau}$ models, where different color lines represent different DM masses. The $U(1)_{\text{D}} \times U(1)_{\text{Y}}$ model (left panel) produces more gamma rays compared to the $U(1)_{\text{D}} \times U(1)_{L_\mu-L_\tau}$ model (right panel) since the mediator A' decaying into quarks and bosons can produce more gamma rays compared to leptonic final states [35].

To better demonstrate how hadronic and leptonic final states shape the energy spectrum, we show a comparison of spectra between these two models and some single annihilation channels in Fig. 7. The energy spectrum of the $U(1)_{\text{D}} \times U(1)_{\text{Y}}$ model exhibits similar characteristics as the

⁴ These dSphs belong to the "Benchmark" samples in [44], including 30 dSphs with measured J-factors from the "Measured" sample, plus additional 12 dSphs that only have J-factor estimates based on the kinematic or photometric scaling relation [47]. 8 "Special" dSphs are excluded for several issues that could affect DM searches.

⁵ https://www-glast.stanford.edu/pub_data/1841/.

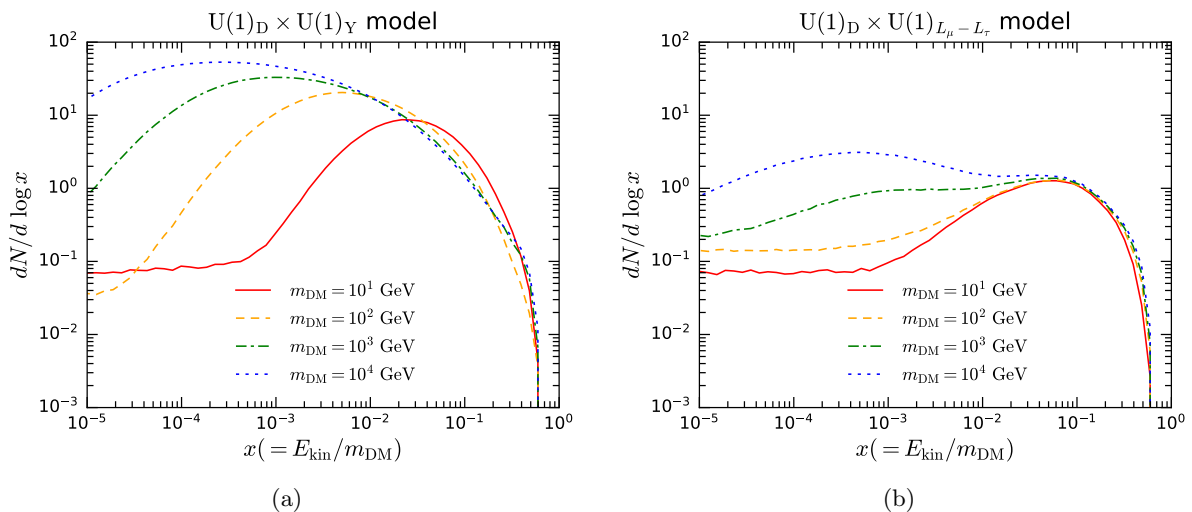


FIG. 6. Gamma-ray spectra for DM annihilates into $A'A'$ for various DM masses: 10 GeV (red), 10² GeV (orange), 10³ GeV (green), and 10⁴ GeV (blue). The left panel presents results for the $U(1)_D \times U(1)_Y$ model, while the right panel shows those for the $U(1)_D \times U(1)_{L_\mu-L_\tau}$ model.

$b\bar{b}$ channel at high energies, reflecting its hadronic decay channels, while mimicking the $V \rightarrow \mu$ channel at low energies due to its leptonic decay channels⁶. In the $U(1)_D \times U(1)_{L_\mu-L_\tau}$ model, since the A' boson decays exclusively into μ pairs, τ pairs, and their corresponding neutrinos, the resulting energy spectrum manifests as a superposition of the $V \rightarrow \mu$ and $V \rightarrow \tau$ channels. Note that the spectrum from $V \rightarrow \tau$ in high energy region is similar to the $b\bar{b}$ channel, which is caused by the hadronic decay processes of tau lepton.

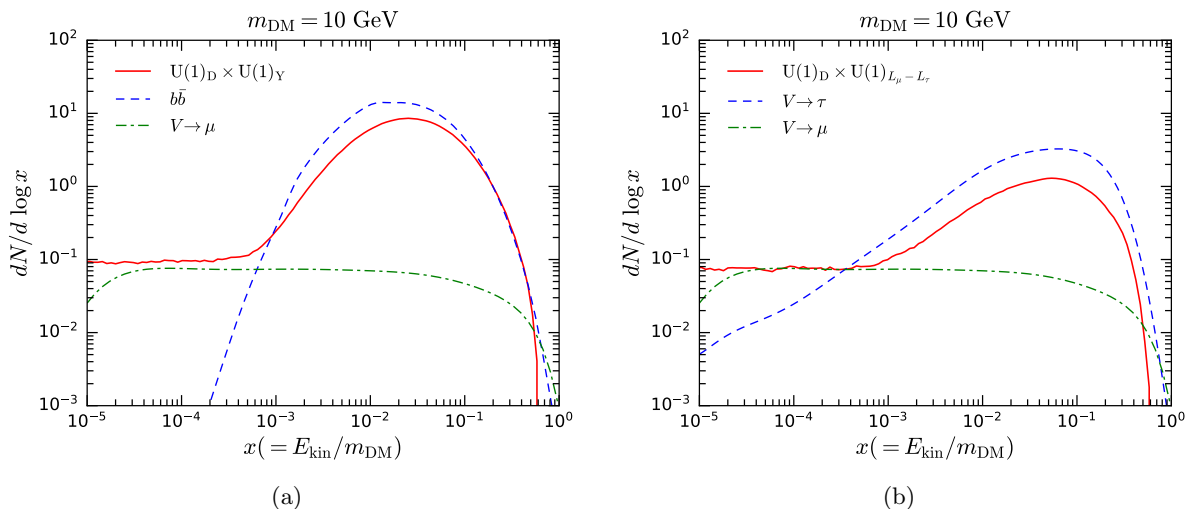


FIG. 7. Gamma-ray spectra for 10 GeV DM annihilating through various channels. Red solid lines represent the total spectra for the $U(1)_D \times U(1)_Y$ model (left panel) and the $U(1)_D \times U(1)_{L_\mu-L_\tau}$ model (right panel). Blue dashed lines show the spectra obtained from $b\bar{b}$ channel (left panel) and from the $V \rightarrow \tau$ channel (right panel), while green dotted-dashed lines represent the spectra from the $V \rightarrow \mu$ channel in both panels.

⁶ $V \rightarrow \mu$ and $V \rightarrow \tau$ represent the processes $2DM \rightarrow 2A' \rightarrow 4\mu$ and $2DM \rightarrow 2A' \rightarrow 4\tau$, respectively

After calculating the gamma-ray flux for the above two models, we now proceed to perform a joint analysis of 42 dSphs using the likelihood functions provided by the Fermi-LAT collaboration. Following the approach outlined in [44], the likelihood function of J-factor is given by,

$$\mathcal{L}(J_i|J_{\text{obs},i},\sigma_i) = \frac{1}{\ln(10)J_{\text{obs},i}\sqrt{2\pi}\sigma_i} e^{-\frac{(\log_{10}(J_i)-\log_{10}(J_{\text{obs},i}))^2}{2\sigma_i^2}}, \quad (24)$$

where J_i represents the true J-factor value for the dSph i , while $J_{\text{obs},i}$ and σ_i denote the observed J-factor and its associated statistical uncertainty, respectively. The values for $J_{\text{obs},i}$ and σ_i are adopted from the analysis presented in [44], which follows the study in [47, 52]. The J-factors of the dSphs and their uncertainties used in our analysis are listed in Table I in Appendix A.

Therefore, we can construct the joint likelihood function as follows:

$$\mathcal{L}(\langle\sigma v\rangle;\mathbf{v}|\mathcal{D}) = \prod_i \mathcal{L}(\langle\sigma v\rangle;J_i,\boldsymbol{\mu}_i|\mathcal{D}) \cdot \mathcal{L}(J_i|J_{\text{obs},i},\sigma_i), \quad (25)$$

where \mathbf{v} represents the nuisance parameters, $\boldsymbol{\mu}_i$ includes any additional nuisance parameter other than J_i , and \mathcal{D} denotes the gamma-ray data. We then perform a test statistic (TS) analysis to determine the one-sided, 95% confidence level (CL) upper limits on $\langle\sigma v\rangle$. This is achieved by identifying a decrease of 2.71/2 in the log-likelihood from its maximum value. To validate our analysis method, we reproduce the 95% CL limits for the $2\text{DM} \rightarrow b\bar{b}$ and $2\text{DM} \rightarrow \tau^+\tau^-$ channels, as shown in Fig. 8. We find an excellent agreement between our results and the limits reported by the Fermi-LAT collaboration.

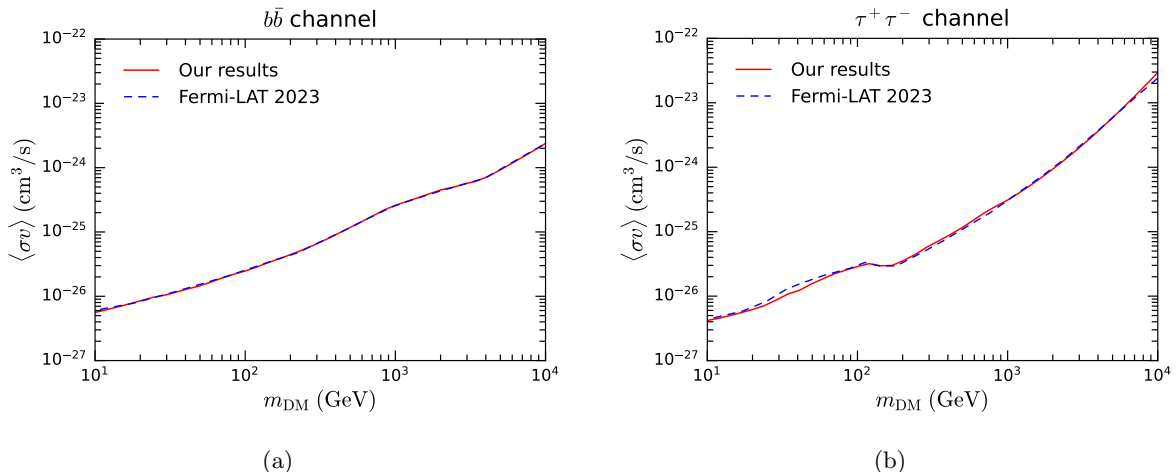


FIG. 8. A comparison of the 95% CL upper limits on $\langle\sigma v\rangle$ for the $b\bar{b}$ (left panel) and $\tau^+\tau^-$ (right panel) channels we obtained (red solid lines), with the results reported by the Fermi-LAT collaboration (blue dashed lines) [44].

B. Cosmic Microwave Background

DM annihilation can inject electromagnetically interacting particles into the thermal bath in early universe, which might affect the anisotropies of Cosmic Microwave Background (CMB) observed by experiments like Planck [34, 53]. This effect is very significant during the cosmic dark ages (corresponding to redshifts $z \sim 20 - 1000$), the period after recombination but before reionization. Photons and e^+e^- pairs produced by DM annihilation, can ionize the ambient hydrogen gas and heat the plasma. This increases the residual ionization fraction, allows free electrons to scatter the CMB photons, and thus broadens the last scattering surface [54–56]. Therefore, the high precision CMB measurements place robust constraints on any energy injection from DM annihilation.

The energy deposited into the gas from DM annihilation can be characterized by a redshift- and model-dependent factor $f(z)$, which is defined as the deposited energy normalized to the energy injected at the same redshift. A portion of this deposited energy contributes to the ionization of the gas, and the final ionizing energy can be expressed as the product of $f(z)$ and the fraction of deposited energy going into ionization. Notably, uncertainties in calculating this fraction can be absorbed into $f(z)$, resulting in a corrected $f(z)$ curve. This is also the approach adopted by the Planck Collaboration.

However, determining $f(z)$ is complicated as it requires tracking the energy loss and interaction processes of high-energy injected particles. A significant advance was made in [57], which provides corrected $f(z)$ curves for DM annihilation into photons and e^+e^- pairs. Performing a principal component analysis (PCA) on $f(z)$ curves, a universal weighting function $W(z)$ was derived to convert $f(z)$ into an effective deposition efficiency $f_{\text{eff}}(E)$ for photons and e^+e^- pairs respectively, and thus the analysis of DM annihilation effects on the CMB is greatly simplified.

Given the energy spectra of positrons $(dN/dE)_{e^+}$ and photons $(dN/dE)_\gamma$, the weighted $f_{\text{eff}}(m_{\text{DM}})$ can be calculated as [58]:

$$f_{\text{eff}}(m_{\text{DM}}) = \frac{1}{2m_{\text{DM}}} \int_0^{m_{\text{DM}}} EdE \left[2f_{\text{eff}}^{e^+e^-}(E) \left(\frac{dN}{dE} \right)_{e^+} + f_{\text{eff}}^\gamma(E) \left(\frac{dN}{dE} \right)_\gamma \right]. \quad (26)$$

The impact of DM annihilations on the CMB can then be characterized by:

$$p_{\text{ann}} = f_{\text{eff}} \frac{\langle \sigma v \rangle}{m_{\text{DM}}}. \quad (27)$$

In 2018, the Planck collaboration has established a 95% C.L. upper limit on p_{ann} after marginalizing over other cosmological parameters [34]:

$$p_{\text{ann}} < 3.2 \times 10^{-28} \text{ cm}^3\text{s}^{-1}\text{GeV}^{-1}. \quad (28)$$

This bound shows considerable improvement compared to the Planck 2015 result, $p_{\text{ann}} < 4.1 \times 10^{-28} \text{ cm}^3\text{s}^{-1}\text{GeV}^{-1}$, primarily due to an enhanced understanding and treatment of polarization systematics in the Planck polarization spectra. To crosscheck our methods with those presented

in [58], we reproduce the CMB constraints on various DM annihilation channels. Fig. 9 presents these constraints for the $b\bar{b}$ (left panel) and $\tau^+\tau^-$ (right panel) channels, showing excellent agreement as well. Note that Ref. [58] used the constraints from Planck 2015 data, whereas our analysis in Sect. IV employs the constraint (28) from Planck 2018 data.

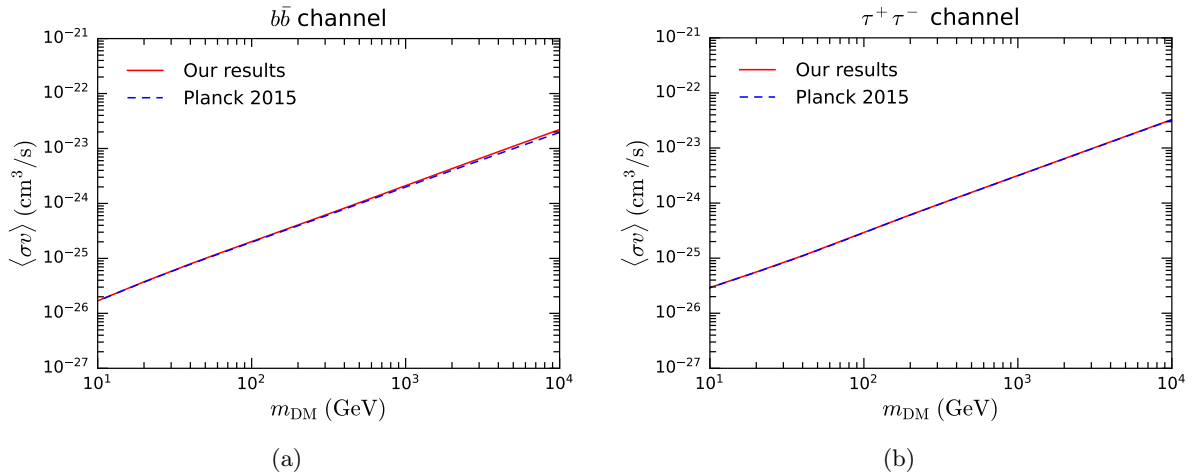


FIG. 9. Comparison of our derived 95% CL upper limits (red) from Planck 2015 result on $\langle\sigma v\rangle$ as a function of m_{DM} for DM annihilation into $b\bar{b}$ (left panel) and $\tau^+\tau^-$ (right panel) with those given by [58] (blue).

IV. RESULTS

In this section, we present the DM relic density, Fermi-LAT and CMB constraints for the $U(1)_{\text{D}} \times U(1)_{\text{Y}}$ -portal and $U(1)_{\text{D}} \times U(1)_{L_{\mu}-L_{\tau}}$ -portal models. Moreover, we apply these constraints to the three types of DM introduced in Sect. II.

In Fig. 10, we provide the constraints on $\langle\sigma v\rangle$ as a function of m_{DM} , which are valid for all spins of DM. The Fermi-LAT 2023 constraints, obtained from a combined analysis of 42 dSphs, are indicated by red solid lines. The Planck 2018 constraints on energy injection into CMB from DM annihilation are indicated by blue solid lines. As a comparison, constraints derived from the assumption of single channel $2\text{DM} \rightarrow b\bar{b}$ (left panel) or $2\text{DM} \rightarrow \tau^+\tau^-$ (right panel) are also presented. Orange dashed lines represent the constraints from Fermi-LAT, while the green dashed lines represent the constraints from the Planck experiment. The updated Planck constraints for these channels are slightly tighter than those presented in Fig. 9 adopted from the Planck 2015 result.

Both panels in Fig. 10 show that the constraints from the Fermi-LAT (gamma rays) are more stringent than those from the Planck (CMB) across the entire mass range. As shown in Fig. 10(a), the Fermi-LAT bounds for the $U(1)_{\text{D}} \times U(1)_{\text{Y}}$ model are looser than the simplified $b\bar{b}$ -channel model in which the final states are purely hadronic. According to Fig. 10(b), we can see that the $U(1)_{\text{D}} \times U(1)_{L_{\mu}-L_{\tau}}$ model performs much better than the simplified $\tau^+\tau^-$ -channel

model since parts of the four-leptons final states consist of neutrinos, which do not radiate photons.

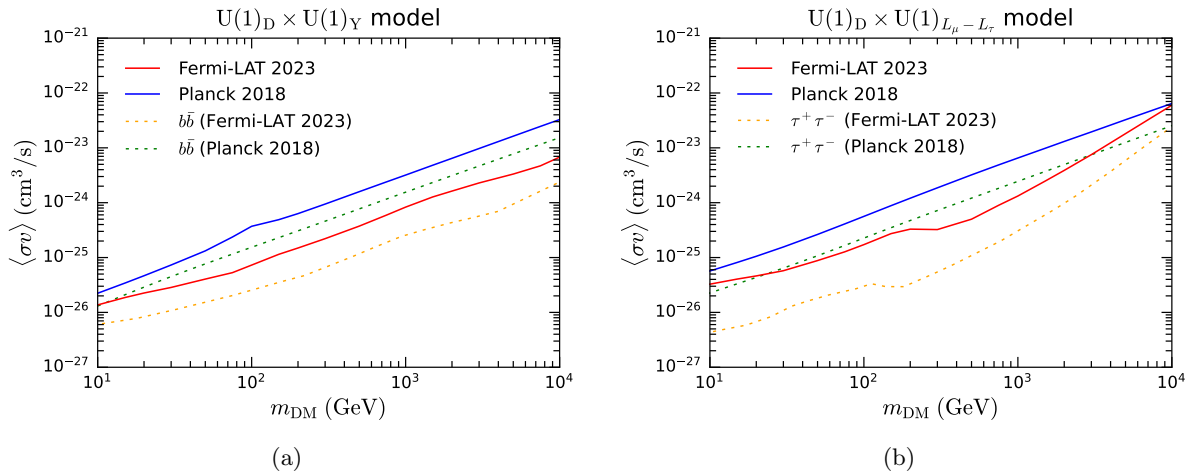


FIG. 10. 95% CL upper limits on $\langle\sigma v\rangle$ as a function of m_{DM} from Fermi-LAT 2023 (red) and Planck 2018 (blue) for the $U(1)_D \times U(1)_Y$ (left) and $U(1)_D \times U(1)_{L_\mu - L_\tau}$ (right) models. Constraints for simplified $b\bar{b}$ -channel (left) and $\tau^+\tau^-$ -channel (right) models from Fermi-LAT (orange) and Planck (green) are also included for comparison

In Fig. 11, we illustrate the upper limits on the gauge coupling g_D for the complex scalar DM model under three different setups of fixed parameters. Gamma-ray (red) and CMB (blue) bounds are depicted, with solid and dashed lines corresponding to the $U(1)_D \times U(1)_Y$ and $U(1)_D \times U(1)_{L_\mu - L_\tau}$ models, respectively. Fig. 11(a) shows the parameter space of g_D versus m_Φ with $r = 1.2$. The green band denotes the parameter space in which the correct DM relic density $\Omega_\Phi h^2 = 0.12$ can be achieved. The green dashed boundary of this region represents the scenario of catalyzed annihilation DM, while the green solid boundary represents the scenario of secluded DM. The intermediate area represents the scenario of semi-catalyzed annihilation, in which the catalyzed annihilation processes are terminated by the decay of A' leading to a sudden freeze-out of DM. The Fig. 5 shown in the previous section, can be regarded as a vertical slice at $m_\Phi = 1000$ GeV, which shows a transition from the catalyzed case to the secluded case as s_ϵ increases, under the assumption of reproducing the correct relic density. Outside the green band, the correct relic density cannot be achieved in any case. Additionally, the gamma-ray and CMB constraints for $U(1)_D \times U(1)_{L_\mu - L_\tau}$ model are milder than the $U(1)_D \times U(1)_Y$ model, as we expect. Specifically, in the $U(1)_D \times U(1)_{L_\mu - L_\tau}$ model, DM mass below ~ 709 GeV is excluded in the catalyzed annihilation scenario, whereas in the $U(1)_D \times U(1)_Y$ model, DM mass has a lower bound ~ 1052 GeV. For the secluded scenario, the constraints on the DM mass are relaxed to ~ 16 GeV and ~ 59 GeV, respectively. Overall, the constraint for the secluded scenario is weaker than those on catalyzed scenario since the latter usually requires a stronger coupling g_D . The constraints for the semi-catalyzed scenario fall within them, depending on the value of s_ϵ ($\Gamma_{A'}$).

Fig. 11(b) shows the parameter space of g_D versus r , with m_Φ to be fixed at 1000 GeV.

As r increases, both the green band and the experiment limits slightly shift downward due to an increase in the annihilation cross section $\langle\sigma_2v\rangle$, which requires a smaller g_D to maintain the correct relic density. For the secluded scenario, the g_D implied by the relic density is far below the Fermi-LAT and CMB bounds in both models. However, for the catalyzed annihilation scenario, the region of $r \gtrsim 1.16(1.48)$ is excluded by the Fermi-LAT data. Note that the curve implied by DM relic density exhibits a different dependence on r compared to the limit curve derived from the Fermi-LAT data. This difference arises because the former is determined by both $\langle\sigma_2v\rangle$ and $\langle\sigma_3v^2\rangle$, whereas the latter depends solely on $\langle\sigma_2v\rangle$. This results in the two curves intersecting at an intermediate point and yields an upper limit of r for the catalyzed annihilation scenario.

The last panel in Fig. 11 shows the relationship between the decay width $\Gamma_{A'}$ and g_D for fixing $m_\Phi = 100$ GeV and $r = 1.2$. The green line represents the parameters which achieve $\Omega_\Phi h^2 = 0.12$. As $\Gamma_{A'}$ increases, DM transits from the catalyzed annihilation case to a secluded case. In the semi-catalyzed region, $\Gamma_{A'}$ and g_D demonstrate an inverse relationship, consistent with Fig. 5. In the secluded and catalyzed regions, further increases or decreases in $\Gamma_{A'}$ no longer influence the final relic density, making the green line vertical to the g_D axis in these regions. Overall, for 100 GeV DM, g_D must lie between 0.19 and 0.39 to ensure the correct relic density. Constraints from gamma rays and CMB are also presented. For $U(1)_D \times U(1)_Y$ and $U(1)_D \times U(1)_{L_\mu-L_\tau}$ models with fixing $m_\Phi = 100$ GeV and $r = 1.2$, the gauge coupling is restricted to be $g_D < 0.22$ (0.28) and 0.34 (0.37) by Fermi-LAT and Planck data, respectively.

Finally, we present the gamma-ray and CMB constraints for fermionic DM (Fig. 12(a)) and vector DM (Fig. 12(c)) DM with fixing $r = 1.2$ as a benchmark. For the Dirac fermion case, in the catalyzed annihilation scenario, the lower limits on the DM mass are ~ 910 GeV in the $U(1)_D \times U(1)_Y$ and ~ 665 GeV in the $U(1)_D \times U(1)_{L_\mu-L_\tau}$ model. In the secluded DM scenario, these limits are determined to be ~ 61 GeV and ~ 17 GeV. In order to compare the results obtained through $2DM \rightarrow 2A' \rightarrow 4SM$ channels and those obtained in previous works using the simplified $2DM \rightarrow 2SM$ channel, we fix the parameter r at $r = 1.45$ and show the limits in Fig. 12(b). In Ref. [20], which considered the $U(1)_D \times U(1)_Y$ model, the Fermi-LAT limits based on $2DM \rightarrow 2SM$ channel analysis are presented. The results adopted from their Fig. 4 showed the bounds for the DM mass to be $m_\chi \gtrsim 2.7$ TeV (catalyzed) and $m_\chi \gtrsim 100$ GeV (secluded) at $r \sim 1.5$. However, our analysis based on $2DM \rightarrow 2A' \rightarrow 4SM$ channels shows that the limits should be modified to $m_\chi \gtrsim 1.4$ TeV (catalyzed) and $m_\chi \gtrsim 55$ GeV (secluded), which are considerably relaxed. The limits for the $U(1)_D \times U(1)_{L_\mu-L_\tau}$ model are even further relaxed, since there is less hadronic decay in this case. Similar conclusions hold for the CMB constraints as well. These results are consistent with our conclusion drawn from the Fig. 10.

For the vector case (Fig. 12(c)), in the catalyzed annihilation scenario, the lower limits on the DM mass is 1086 GeV in the $U(1)_D \times U(1)_Y$ and 706 GeV in the $U(1)_D \times U(1)_{L_\mu-L_\tau}$ model. In contrast, Ref. [21], which is based on the limits obtained by $2DM \rightarrow 2SM$ channel, excludes the catalyzed annihilation vector DM from $U(1)_D \times U(1)_Y$ model with a mass below ~ 4.4 TeV when $r = 1.2$ (see their Fig. 4). The refined analysis based on $2DM \rightarrow 2A' \rightarrow 4SM$ channels in

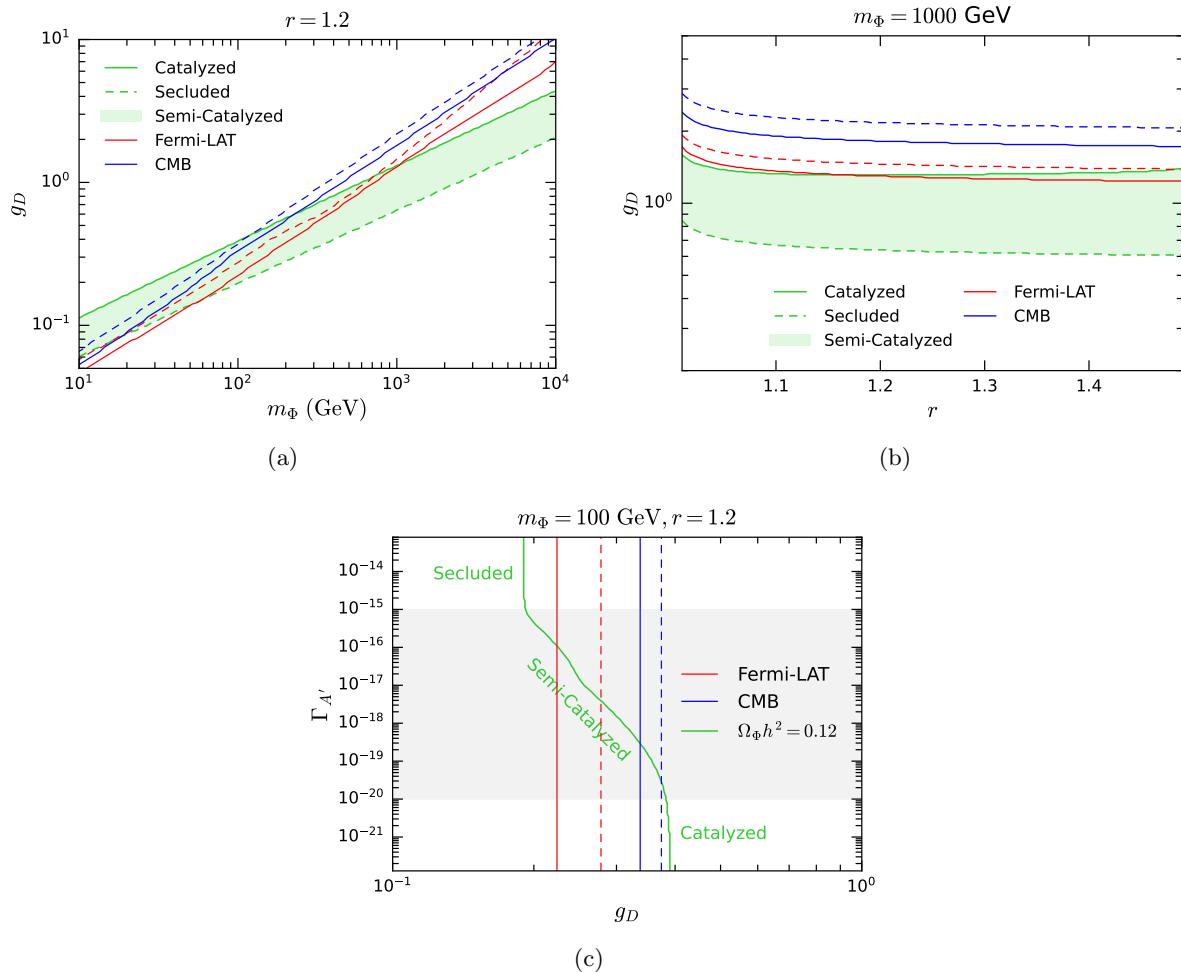


FIG. 11. Parameter spaces for complex scalar DM. The first panel shows g_D versus m_Φ with $r = 1.2$, while the second panel shows g_D versus r with $m_\Phi = 1000$ GeV. The last panel shows the relationship between $\Gamma_{A'}$ and g_D for $m_\Phi = 100$ GeV and $r = 1.2$. The green areas (upper panels) and the green curve (below panel) represent the region satisfying $\Omega_\Phi h^2 = 0.12$. The red and blue curves represent the Fermi-LAT and CMB constraints, with the solid and dashed ones corresponding to the $U(1)_D \times U(1)_Y$ and $U(1)_D \times U(1)_{L_\mu - L_\tau}$ models, respectively.

this work significantly relax the constraints.

V. CONCLUSIONS

In this work, we have proposed a complex scalar dark matter model based on a hidden $U(1)_D$ gauge symmetry. The complex scalar Φ charged under $U(1)_D$ serves as the DM candidate while the new gauge boson A' plays the role of mediator bridging the dark and the SM sectors via a kinetic mixing. We focus on a situation that the mass ratio of DM and A' , r , is within a range $1 \lesssim r \lesssim 1.5$. In this case, the most relevant annihilation processes for DM density evolution are $2\Phi \rightarrow 2A'$ and $3A' \rightarrow 2\Phi$. Depending on the decay width of A' , the freeze-out scenarios of DM can be various. To be precise, when $\Gamma_{A'}$ is small enough, the catalyzed annihilation

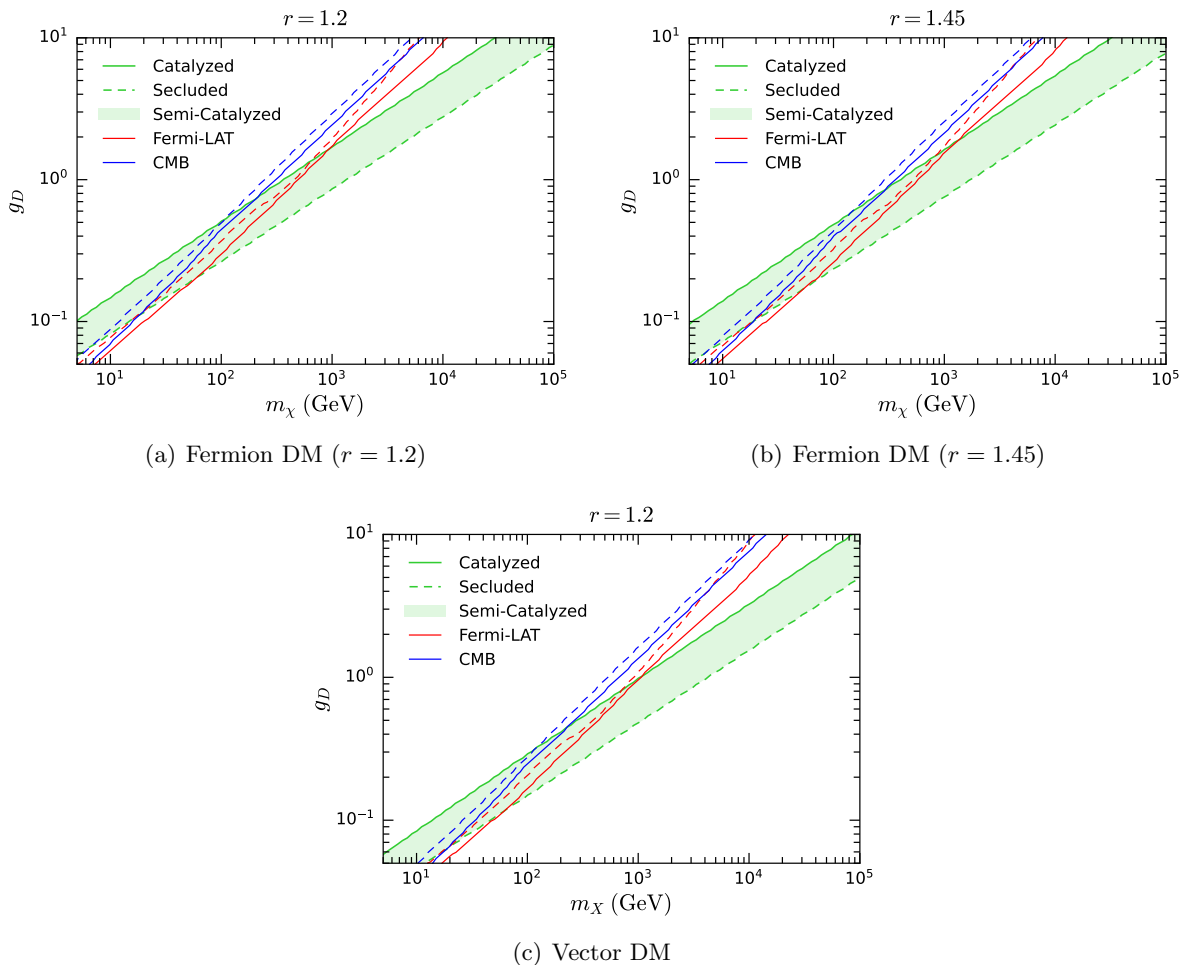


FIG. 12. Fermi-LAT and CMB constraints for fermionic and vector DM.

processes proceed until DM freeze-out. On the other hand, if $\Gamma_{A'}$ is large enough, A' maintains thermal equilibrium and $3A' \rightarrow 2\Phi$ can be neglected, resulting in a usual freeze-out scenario of the secluded DM model. Between these two limits, the catalyzed annihilation processes can proceed until A' decays, so we call it a semi-catalyzed scenario.

We have calculated the annihilation cross sections for the $2\Phi \rightarrow 2A'$ and $3A' \rightarrow 2\Phi$ processes, and determined the DM phenomenology including relic density, indirect detection (gamma-ray detection of Fermi-LAT), and CMB (Planck). Since the dark sector couples to the SM sector feebly, the stringent direct detection bound can be easily circumvented, and thus the indirect searching is the most important way to detect DM. For comprehensiveness, we also consider the relic density and indirect detection constraints on the fermionic and vector DM models.

We have studied two models with different portals connecting the dark sector to SM: $U(1)_D \times U(1)_Y$ and $U(1)_D \times U(1)_{L_\mu - L_\tau}$. The former kinetically mixes A' with the hypercharge gauge field B , while the latter mixes it with a new gauge boson Z' originating from a $U(1)_{L_\mu - L_\tau}$ gauge symmetry. The $U(1)_D \times U(1)_Y$ model enables A' to decay into quarks and leptons, and thus more gamma rays are produced comparing to the $U(1)_D \times U(1)_{L_\mu - L_\tau}$ model, which has less hadronic

decay processes. We obtain the Fermi-LAT constraints from a combined analysis of 14.3 years of observations on 42 dSphs, and the CMB constraints from Planck experimental results of DM annihilation into photons and electron-positron pairs during the cosmic dark ages.

Finally, we present the relic density and indirect detection constraints for the $U(1)_D \times U(1)_Y$ and $U(1)_D \times U(1)_{L_\mu-L_\tau}$ models with different DM spins, and find viable parameter space for all cases. Since the dominant annihilation processes for DM are $2DM \rightarrow 2A' \rightarrow 4SM$ in our models, we find that both models have much weaker bounds on the $\langle\sigma v\rangle$ compared to the previous analysis based on the $2DM \rightarrow 2SM$ channels. Additionally, limits for $U(1)_D \times U(1)_Y$ are more stringent than those for $U(1)_D \times U(1)_{L_\mu-L_\tau}$ as we expected. For complex scalar DM with a mass ratio of $r = 1.2$ between the DM and the mediator, a DM heavier than 709 GeV (16 GeV) in the catalyzed annihilation (secluded) scenario remains available under all constraints. For the fermionic and vector DM, our limits are more relaxed than previous studies using single-channel bounds. For instance, fermionic DM with $m_\chi \sim 1$ TeV in the catalyzed annihilation scenario, which was excluded in the previous study, now remains available under the $U(1)_D \times U(1)_{L_\mu-L_\tau}$ framework. For the vector DM with $r = 1.2$, the Fermi-LAT limit is relaxed from ~ 4.4 TeV to 706 GeV in the catalyzed annihilation scenario.

ACKNOWLEDGMENTS

C. C. is supported by the National Natural Science Foundation of China (NSFC) under Grant No. 11905300, and the Guangzhou Science and Technology Planning Project under Grant No. 2023A04J0008. H.-H. Z. is supported by the NSFC under Grant No. 12275367. This work is also supported by the Fundamental Research Funds for the Central Universities, and the Sun Yat-Sen University Science Foundation.

Appendix A: J-factors for the Benchmark Sample

Name	R.A. (J2000) [deg]	Decl. (J2000) [deg]	Distance [kpc]	$\log_{10} J \pm \sigma_J$ [$\log_{10} \text{GeV}^2 \text{cm}^{-5}$]
Aquarius II	338.48	-9.33	108.0	17.80 ± 0.55
Boötes II	209.51	12.86	42.0	18.30 ± 0.95
Canes Venatici I	202.01	33.55	218.0	17.42 ± 0.16
Canes Venatici II	194.29	34.32	160.0	17.82 ± 0.47
Carina	100.41	-50.96	105.0	17.83 ± 0.10
Carina II	114.11	-58.0	36.0	18.25 ± 0.55
Coma Berenices	186.75	23.91	44.0	19.00 ± 0.35
Draco	260.07	57.92	76.0	18.83 ± 0.12
Draco II	238.17	64.58	22.0	18.93 ± 1.54
Eridanus II	56.09	-43.53	380.0	16.60 ± 0.90
Fornax	39.96	-34.5	147.0	18.09 ± 0.10
Grus I	344.18	-50.18	120.0	16.50 ± 0.80
Hercules	247.77	12.79	132.0	17.37 ± 0.53

Horologium I	43.88	-54.12	79.0	19.00 ± 0.81
Hydrus I	37.39	-79.31	28.0	18.33 ± 0.36
Leo I	152.11	12.31	254.0	17.64 ± 0.13
Leo II	168.36	22.15	233.0	17.76 ± 0.20
Leo IV	173.24	-0.55	154.0	16.40 ± 1.08
Leo V	172.79	2.22	178.0	17.65 ± 0.97
Pegasus III	336.1	5.41	215.0	18.30 ± 0.93
Pisces II	344.63	5.95	182.0	17.30 ± 1.04
Reticulum II	53.92	-54.05	30.0	18.90 ± 0.38
Sagittarius II	298.16	-22.07	69.0	17.35 ± 1.36
Segue 1	151.75	16.08	23.0	19.12 ± 0.53
Sextans	153.26	-1.61	86.0	17.73 ± 0.12
Tucana II	342.98	-58.57	58.0	18.97 ± 0.54
Tucana IV	0.73	-60.85	48.0	18.40 ± 0.55
Ursa Major I	158.77	51.95	97.0	18.26 ± 0.28
Ursa Major II	132.87	63.13	32.0	19.44 ± 0.40
Ursa Minor	227.24	67.22	76.0	18.75 ± 0.12
Boötes IV	233.69	43.73	209.0	17.25 ± 0.60
Carina III	114.63	-57.79	28.0	19.70 ± 0.60
Centaurus I	189.59	-40.9	116.0	18.14 ± 0.60
Cetus II	19.47	-17.42	30.0	19.10 ± 0.60
Cetus III	31.33	-4.27	251.0	17.30 ± 0.60
Columba I	82.86	-28.01	183.0	17.60 ± 0.60
Grus II	331.02	-46.44	53.0	18.40 ± 0.60
Phoenix II	355.0	-54.41	83.0	18.30 ± 0.60
Pictor I	70.95	-50.29	114.0	18.00 ± 0.60
Pictor II	101.18	-59.9	46.0	18.83 ± 0.60
Reticulum III	56.36	-60.45	92.0	18.20 ± 0.60
Tucana V	354.35	-63.27	55.0	18.90 ± 0.60

TABLE I: Properties of 42 dSphs used in our analysis, including coordinates (R.A. and Decl.), distances, and J-factor values for each galaxy [44].

Appendix B: Kinetic Equilibrium Before DM Freeze-out

A template approach to maintaining the kinetic equilibrium of DM is to refer to the method proposed in section II.B of Ref. [15]. We assume DM couples to a new scalar field Ψ , which is relativistic before the freeze-out of DM. Ψ particle should be unstable and decay into SM particles after the freeze-out of DM. If we want DM to maintain kinetic equilibrium while ensuring that the evolution of its density is negligibly affected by this interaction, then the following conditions should be imposed:

1. The interaction must be strong enough to maintain DM in kinetic equilibrium until freeze-out.

2. The new annihilation cross section of $2\Phi \rightarrow 2\Psi$ must be sufficiently small to avoid altering the thermal evolution of DM described in Sect. II.

The interaction between Φ and Ψ fields can be the following quartic term:

$$\mathcal{L}_{\Phi\Psi} = \lambda_{\Phi\Psi} |\Phi|^2 |\Psi|^2. \quad (\text{B1})$$

The thermally averaged cross section for the processes $2\Phi \rightarrow 2\Psi$ and $\Phi\Psi \rightarrow \Phi\Psi$ can be easily derived as:

$$\langle\sigma v\rangle_{2\Phi\rightarrow 2\Psi} = \frac{\lambda_{\Phi\Psi}^2}{32\pi m_\Phi^2}, \quad \langle\sigma v\rangle_{\Phi\Psi\rightarrow\Phi\Psi} = \frac{\lambda_{\Phi\Psi}^2}{16\pi m_\Phi^2} \quad (\text{B2})$$

Then the 1st. condition can be estimated by [21, 59, 60],

$$\frac{T}{m_\Phi} \frac{n_\Psi \langle\sigma_{\Phi\Psi\rightarrow\Phi\Psi}\rangle}{H} \gtrsim 1, \quad (\text{B3})$$

where H is the Hubble constant and n_Ψ denotes the number density of Ψ . Fig. 13 illustrates the allowed parameter space for $\lambda_{\Phi\Psi}$ as a function of m_{DM} , satisfying both conditions. We fix the mass ratio between DM and mediator A' at 1.2, while g_D varies with m_{DM} to ensure the correct relic density. The regions above the red curves satisfy relation (B3), with solid and dashed curves corresponding to the catalyzed annihilation and secluded scenarios, respectively. We define $\eta = \langle\sigma_{2v}\rangle_{2\Phi\rightarrow 2\Psi} / \langle\sigma_{2v}\rangle_{2\Phi\rightarrow 2A'}$, with blue curves indicating $\eta = 0.1$. In the regions below the blue curves, the annihilation cross section for the $2\Phi \rightarrow 2\Psi$ process accounts for less than 10% of the total quantity, so it is negligible. We find that it is easy to ensure the kinetic equilibrium of DM if $\lambda_{\Phi\Psi} \sim 10^{-3}$ in both scenarios. For the fermionic and vector dark matter, the interactions between DM and Ψ can be achieved by non-renormalizable operators (see Ref. [15] as an example for the fermionic case).

-
- [1] G. Jungman, M. Kamionkowski, and K. Griest, ‘‘Supersymmetric dark matter,’’ *Phys. Rept.* **267** (1996) 195–373, [arXiv:hep-ph/9506380](#).
 - [2] G. Bertone, D. Hooper, and J. Silk, ‘‘Particle dark matter: Evidence, candidates and constraints,’’ *Phys. Rept.* **405** (2005) 279–390, [arXiv:hep-ph/0404175](#).
 - [3] J. L. Feng, ‘‘Dark Matter Candidates from Particle Physics and Methods of Detection,’’ *Ann. Rev. Astron. Astrophys.* **48** (2010) 495–545, [arXiv:1003.0904](#) [[astro-ph.CO](#)].
 - [4] M. Bauer and T. Plehn, *Yet Another Introduction to Dark Matter: The Particle Physics Approach*, vol. 959 of *Lecture Notes in Physics*. Springer, 2019. [arXiv:1705.01987](#) [[hep-ph](#)].
 - [5] B. W. Lee and S. Weinberg, ‘‘Cosmological Lower Bound on Heavy Neutrino Masses,’’ *Phys. Rev. Lett.* **39** (1977) 165–168.
 - [6] **XENON** Collaboration, E. Aprile *et al.*, ‘‘First Dark Matter Search with Nuclear Recoils from the XENONnT Experiment,’’ *Phys. Rev. Lett.* **131** (2023) 041003, [arXiv:2303.14729](#) [[hep-ex](#)].
 - [7] **PandaX** Collaboration, Z. Bo *et al.*, ‘‘Dark Matter Search Results from 1.54 Tonne-Year Exposure of PandaX-4T,’’ *Phys. Rev. Lett.* **134** (2025) 011805, [arXiv:2408.00664](#) [[hep-ex](#)].

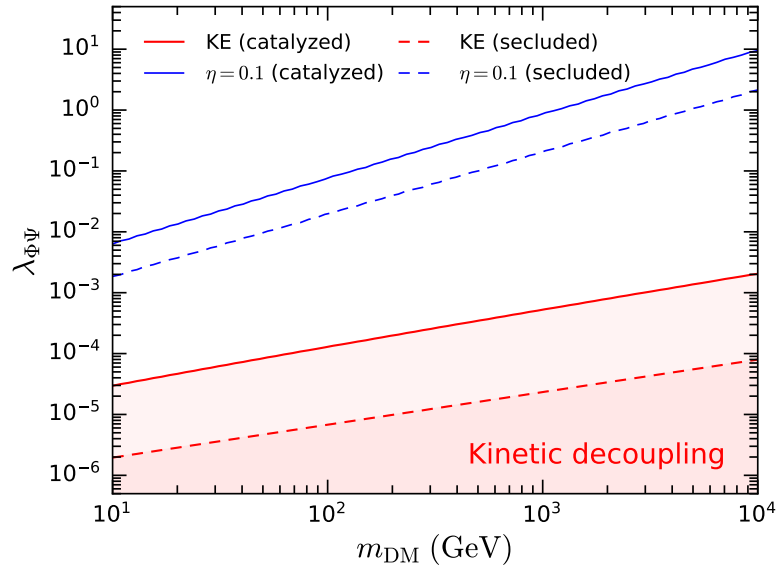


FIG. 13. Parameter space for $\lambda_{\Phi\Psi}$ versus m_{DM} , where the viable region lies between the KE condition bound (red curves) and $\eta = 0.1$ bound (blue curves) for both catalyzed annihilation (solid) and secluded (dashed) scenarios.

- [8] **LZ** Collaboration, J. Aalbers *et al.*, “Dark Matter Search Results from 4.2 Tonne-Years of Exposure of the LUX-ZEPLIN (LZ) Experiment,” [arXiv:2410.17036 \[hep-ex\]](#).
- [9] G. Arcadi, M. Dutra, P. Ghosh, M. Lindner, Y. Mambrini, M. Pierre, S. Profumo, and F. S. Queiroz, “The waning of the WIMP? A review of models, searches, and constraints,” *Eur. Phys. J. C* **78** (2018) 203, [arXiv:1703.07364 \[hep-ph\]](#).
- [10] L. Roszkowski, E. M. Sessolo, and S. Trojanowski, “WIMP dark matter candidates and searches—current status and future prospects,” *Rept. Prog. Phys.* **81** (2018) 066201, [arXiv:1707.06277 \[hep-ph\]](#).
- [11] Y. Hochberg, E. Kuflik, T. Volansky, and J. G. Wacker, “Mechanism for Thermal Relic Dark Matter of Strongly Interacting Massive Particles,” *Phys. Rev. Lett.* **113** (2014) 171301, [arXiv:1402.5143 \[hep-ph\]](#).
- [12] Y. Hochberg, E. Kuflik, H. Murayama, T. Volansky, and J. G. Wacker, “Model for Thermal Relic Dark Matter of Strongly Interacting Massive Particles,” *Phys. Rev. Lett.* **115** (2015) 021301, [arXiv:1411.3727 \[hep-ph\]](#).
- [13] J. Smirnov and J. F. Beacom, “New Freezeout Mechanism for Strongly Interacting Dark Matter,” *Phys. Rev. Lett.* **125** (2020) 131301, [arXiv:2002.04038 \[hep-ph\]](#).
- [14] R. T. D’Agnolo and J. T. Ruderman, “Light Dark Matter from Forbidden Channels,” *Phys. Rev. Lett.* **115** (2015) 061301, [arXiv:1505.07107 \[hep-ph\]](#).
- [15] J. M. Cline, H. Liu, T. Slatyer, and W. Xue, “Enabling Forbidden Dark Matter,” *Phys. Rev. D* **96** (2017) 083521, [arXiv:1702.07716 \[hep-ph\]](#).
- [16] P. J. Fitzpatrick, H. Liu, T. R. Slatyer, and Y.-D. Tsai, “New pathways to the relic abundance of vector-portal dark matter,” *Phys. Rev. D* **106** (2022) 083517, [arXiv:2011.01240 \[hep-ph\]](#).
- [17] M. Pospelov, A. Ritz, and M. B. Voloshin, “Secluded WIMP Dark Matter,” *Phys. Lett. B* **662** (2008) 53–61, [arXiv:0711.4866 \[hep-ph\]](#).
- [18] M. Pospelov, “Secluded U(1) below the weak scale,” *Phys. Rev. D* **80** (2009) 095002, [arXiv:0811.1030 \[hep-ph\]](#).

- [19] M. Pospelov and A. Ritz, “Astrophysical Signatures of Secluded Dark Matter,” *Phys. Lett. B* **671** (2009) 391–397, [arXiv:0810.1502 \[hep-ph\]](#).
- [20] C.-Y. Xing and S.-H. Zhu, “Dark Matter Freeze-Out via Catalyzed Annihilation,” *Phys. Rev. Lett.* **127** (2021) 061101, [arXiv:2102.02447 \[hep-ph\]](#).
- [21] C. Cai and H.-H. Zhang, “Vector dark matter production from catalyzed annihilation,” *JHEP* **01** (2022) 099, [arXiv:2107.13475 \[hep-ph\]](#).
- [22] A. Berlin, D. Hooper, and S. D. McDermott, “Simplified Dark Matter Models for the Galactic Center Gamma-Ray Excess,” *Phys. Rev. D* **89** (2014) 115022, [arXiv:1404.0022 \[hep-ph\]](#).
- [23] H. Wu and S. Zheng, “Scalar Dark Matter: Real vs Complex,” *JHEP* **03** (2017) 142, [arXiv:1610.06292 \[hep-ph\]](#).
- [24] C.-R. Chen, Y.-X. Lin, C. S. Nugroho, R. Ramos, Y.-L. S. Tsai, and T.-C. Yuan, “Complex scalar dark matter in the gauged two-Higgs-doublet model,” *Phys. Rev. D* **101** (2020) 035037, [arXiv:1910.13138 \[hep-ph\]](#).
- [25] J. Lao, C. Cai, Z.-H. Yu, Y.-P. Zeng, and H.-H. Zhang, “Fermionic and scalar dark matter with hidden U(1) gauge interaction and kinetic mixing,” *Phys. Rev. D* **101** (2020) 095031, [arXiv:2003.02516 \[hep-ph\]](#).
- [26] Y.-H. Su, C. Cai, Y.-P. Zeng, and H.-H. Zhang, “Complex scalar dark matter in a new gauged U(1) symmetry with kinetic and direct mixings,” *Phys. Rev. D* **110** (2024) 095014, [arXiv:2406.18170 \[hep-ph\]](#).
- [27] S. Profumo, F. S. Queiroz, J. Silk, and C. Siqueira, “Searching for Secluded Dark Matter with H.E.S.S., Fermi-LAT, and Planck,” *JCAP* **03** (2018) 010, [arXiv:1711.03133 \[hep-ph\]](#).
- [28] C. Siqueira, “Secluded Dark Matter in light of the Cherenkov Telescope Array (CTA),” *Phys. Lett. B* **797** (2019) 134840, [arXiv:1901.11055 \[hep-ph\]](#).
- [29] C. Siqueira, G. N. Fortes, A. Viana, and F. S. Queiroz, “Indirect Searches for Secluded Dark Matter,” *PoS ICRC2021* (2021) 577, [arXiv:2107.04053 \[hep-ph\]](#).
- [30] G. N. Fortes, F. S. Queiroz, C. Siqueira, and A. Viana, “Present and future constraints on secluded dark matter in the Galactic Halo with TeV Gamma-ray observatories,” *JCAP* **07** (2023) 043, [arXiv:2212.05075 \[hep-ph\]](#).
- [31] J.-M. Zheng, Z.-H. Yu, J.-W. Shao, X.-J. Bi, Z. Li, and H.-H. Zhang, “Constraining the interaction strength between dark matter and visible matter: I. fermionic dark matter,” *Nucl. Phys. B* **854** (2012) 350–374, [arXiv:1012.2022 \[hep-ph\]](#).
- [32] Z.-H. Yu, J.-M. Zheng, X.-J. Bi, Z. Li, D.-X. Yao, and H.-H. Zhang, “Constraining the interaction strength between dark matter and visible matter: II. scalar, vector and spin-3/2 dark matter,” *Nucl. Phys. B* **860** (2012) 115–151, [arXiv:1112.6052 \[hep-ph\]](#).
- [33] E. Gabrielli, L. Marzola, M. Raidal, and H. Veermäe, “Dark matter and spin-1 milli-charged particles,” *JHEP* **08** (2015) 150, [arXiv:1507.00571 \[hep-ph\]](#).
- [34] **Planck** Collaboration, N. Aghanim *et al.*, “Planck 2018 results. VI. Cosmological parameters,” *Astron. Astrophys.* **641** (2020) A6, [arXiv:1807.06209 \[astro-ph.CO\]](#). [Erratum: *Astron. Astrophys.* 652, C4 (2021)].
- [35] M. Cirelli, G. Corcella, A. Hektor, G. Hutsi, M. Kadastik, P. Panci, M. Raidal, F. Sala, and A. Strumia, “PPPC 4 DM ID: A Poor Particle Physicist Cookbook for Dark Matter Indirect Detection,” *JCAP* **03** (2011) 051, [arXiv:1012.4515 \[hep-ph\]](#). [Erratum: *JCAP* 10, E01 (2012)].
- [36] C. Bierlich *et al.*, “A comprehensive guide to the physics and usage of PYTHIA 8.3,” *SciPost Phys. Codeb.* **2022** (2022) 8, [arXiv:2203.11601 \[hep-ph\]](#).
- [37] A. Bodas, R. Coy, and S. J. D. King, “Solving the electron and muon $g - 2$ anomalies in Z' models,” *Eur. Phys. J. C* **81** (2021) 1065, [arXiv:2102.07781 \[hep-ph\]](#).

- [38] P. Panda, M. K. Behera, P. Mishra, and R. Mohanta, “Unveiling neutrino phenomenology, $(g-2)_e, \mu$ and leptogenesis through $U(1)$ gauge symmetries in an inverse seesaw model,” *Phys. Rev. D* **108** (2023) 035032, [arXiv:2203.14536 \[hep-ph\]](#).
- [39] D. Borah, M. Dutta, S. Mahapatra, and N. Sahu, “Lepton anomalous magnetic moment with singlet-doublet fermion dark matter in a scotogenic $U(1)_{L\mu-L\tau}$ model,” *Phys. Rev. D* **105** (2022) 015029, [arXiv:2109.02699 \[hep-ph\]](#).
- [40] G. Grilli di Cortona and E. Nardi, “Probing light mediators at the MUonE experiment,” *Phys. Rev. D* **105** (2022) L111701, [arXiv:2204.04227 \[hep-ph\]](#).
- [41] G. H. Duan, X.-G. He, L. Wu, and J. M. Yang, “Leptophilic dark matter in gauged $U(1)_{L_e-L_\mu}$ model in light of DAMPE cosmic ray $e^+ + e^-$ excess,” *Eur. Phys. J. C* **78** (2018) 323, [arXiv:1711.11563 \[hep-ph\]](#).
- [42] X.-G. He, “Dark Matter Annihilation Explanation for e^+ Excesses in Cosmic Ray,” *Mod. Phys. Lett. A* **24** (2009) 2139–2160, [arXiv:0908.2908 \[hep-ph\]](#).
- [43] **Fermi-LAT** Collaboration, M. Ackermann *et al.*, “Searching for Dark Matter Annihilation from Milky Way Dwarf Spheroidal Galaxies with Six Years of Fermi Large Area Telescope Data,” *Phys. Rev. Lett.* **115** (2015) 231301, [arXiv:1503.02641 \[astro-ph.HE\]](#).
- [44] A. McDaniel, M. Ajello, C. M. Karwin, M. Di Mauro, A. Drlica-Wagner, and M. A. Sánchez-Conde, “Legacy analysis of dark matter annihilation from the Milky Way dwarf spheroidal galaxies with 14 years of Fermi-LAT data,” *Phys. Rev. D* **109** (2024) 063024, [arXiv:2311.04982 \[astro-ph.HE\]](#).
- [45] **MAGIC, Fermi-LAT** Collaboration, M. L. Ahnen *et al.*, “Limits to Dark Matter Annihilation Cross-Section from a Combined Analysis of MAGIC and Fermi-LAT Observations of Dwarf Satellite Galaxies,” *JCAP* **02** (2016) 039, [arXiv:1601.06590 \[astro-ph.HE\]](#).
- [46] S. Profumo, F. S. Queiroz, and C. E. Yaguna, “Extending Fermi-LAT and H.E.S.S. Limits on Gamma-ray Lines from Dark Matter Annihilation,” *Mon. Not. Roy. Astron. Soc.* **461** (2016) 3976–3981, [arXiv:1602.08501 \[astro-ph.HE\]](#).
- [47] A. B. Pace and L. E. Strigari, “Scaling Relations for Dark Matter Annihilation and Decay Profiles in Dwarf Spheroidal Galaxies,” *Mon. Not. Roy. Astron. Soc.* **482** (2019) 3480–3496, [arXiv:1802.06811 \[astro-ph.GA\]](#).
- [48] J. F. Navarro, C. S. Frenk, and S. D. M. White, “A Universal density profile from hierarchical clustering,” *Astrophys. J.* **490** (1997) 493–508, [arXiv:astro-ph/9611107](#).
- [49] A. W. Graham, D. Merritt, B. Moore, J. Diemand, and B. Terzic, “Empirical models for Dark Matter Halos. I. Nonparametric Construction of Density Profiles and Comparison with Parametric Models,” *Astron. J.* **132** (2006) 2685–2700, [arXiv:astro-ph/0509417](#).
- [50] A. Burkert, “The Structure of dark matter halos in dwarf galaxies,” *Astrophys. J. Lett.* **447** (1995) L25, [arXiv:astro-ph/9504041](#).
- [51] P. Salucci and A. Burkert, “Dark matter scaling relations,” *Astrophys. J. Lett.* **537** (2000) L9–L12, [arXiv:astro-ph/0004397](#).
- [52] **DES** Collaboration, A. Drlica-Wagner *et al.*, “Milky Way Satellite Census. I. The Observational Selection Function for Milky Way Satellites in DES Y3 and Pan-STARRS DR1,” *Astrophys. J.* **893** (2020) 1, [arXiv:1912.03302 \[astro-ph.GA\]](#).
- [53] **Planck** Collaboration, P. A. R. Ade *et al.*, “Planck 2015 results. XIII. Cosmological parameters,” *Astron. Astrophys.* **594** (2016) A13, [arXiv:1502.01589 \[astro-ph.CO\]](#).
- [54] J. A. Adams, S. Sarkar, and D. W. Sciama, “CMB anisotropy in the decaying neutrino cosmology,” *Mon. Not. Roy. Astron. Soc.* **301** (1998) 210–214, [arXiv:astro-ph/9805108](#).
- [55] X.-L. Chen and M. Kamionkowski, “Particle decays during the cosmic dark ages,” *Phys. Rev. D* **70**

- (2004) 043502, [arXiv:astro-ph/0310473](#).
- [56] N. Padmanabhan and D. P. Finkbeiner, “Detecting dark matter annihilation with CMB polarization: Signatures and experimental prospects,” *Phys. Rev. D* **72** (2005) 023508, [arXiv:astro-ph/0503486](#).
- [57] T. R. Slatyer, “Indirect Dark Matter Signatures in the Cosmic Dark Ages II. Ionization, Heating and Photon Production from Arbitrary Energy Injections,” *Phys. Rev. D* **93** (2016) 023521, [arXiv:1506.03812 \[astro-ph.CO\]](#).
- [58] T. R. Slatyer, “Indirect dark matter signatures in the cosmic dark ages. I. Generalizing the bound on s-wave dark matter annihilation from Planck results,” *Phys. Rev. D* **93** (2016) 023527, [arXiv:1506.03811 \[hep-ph\]](#).
- [59] S. Hofmann, D. J. Schwarz, and H. Stoecker, “Damping scales of neutralino cold dark matter,” *Phys. Rev. D* **64** (2001) 083507, [arXiv:astro-ph/0104173](#).
- [60] L. Visinelli and P. Gondolo, “Kinetic decoupling of WIMPs: analytic expressions,” *Phys. Rev. D* **91** (2015) 083526, [arXiv:1501.02233 \[astro-ph.CO\]](#).